HHS Public Access

Author manuscript

Sci Signal. Author manuscript; available in PMC 2017 September 08.

Published in final edited form as:

Sci Signal. ; 10(473): . doi:10.1126/scisignal.aai7696.

Astrocyte-shed extracellular vesicles regulate the peripheral leukocyte response to inflammatory brain lesions

Alex M. Dickens[1,*], **Luis B. Tovar-y-Romo**[1,*], **Seung-Wan Yoo**[1], **Amanda L. Trout**[1], **Mihyun Bae**[1], **Marlene Kanmogne**[1], **Bezawit Megra**[2], **Dionna W. Williams**[2], **Kennith W. Witwer**[3], **Mar Gacias**[4], **Nino Tabatadze**[1], **Robert N. Cole**[5], **Patrizia Casaccia**[4], **Joan W. Berman**[2], **Daniel C. Anthony**[6], and **Norman J. Haughey**[1,7,†]

[1]Department of Neurology, Johns Hopkins University School of Medicine, Baltimore, MD 21287, USA

[2]Departments of Pathology, Microbiology, and Immunology, Albert Einstein College of Medicine, Bronx, NY 10461, USA

[3]Department of Molecular and Comparative Pathobiology, Johns Hopkins University School of Medicine, Baltimore, MD 21287, USA

[4]Department of Neuroscience, Genetics and Genomics, Icahn School of Medicine at Mount Sinai, New York, NY 10029, USA

[5]Department of Biological Chemistry, Johns Hopkins University School of Medicine, Baltimore, MD 21287, USA

[6]Department of Pharmacology, University of Oxford, Oxford OX1 3QT, U.K.

[7]Department of Psychiatry, Johns Hopkins University School of Medicine, Baltimore, MD 21287, USA

Abstract

Brain injury induces a peripheral acute cytokine response that directs the transmigration of leukocytes into the brain. Because this brain-to-peripheral immune communication affects patient recovery, understanding its regulation is important. Using a mouse model of inflammatory brain

†Corresponding author: nhaughe1@jhmi.edu.
*These authors contributed equally to this work.

SUPPLEMENTARY MATERIALS

www.sciencesignaling.org/cgi/content/full/10/473/eaai7696/DC1

Author contributions: The study was designed by N.J.H. All in vivo work was performed by A.M.D., L.B.T., S.-W.Y., and D.C.A. Cell culture experiments were performed by A.L.T. and L.B.T. Exosome isolations were performed by A.L.T. and L.B.T. A.L.T. performed all RT-PCR experiments. Immunohistochemistry, Western blot experiments, and quantification were performed by A.M.D., L.B.T., A.L.T., M.K., N.T., M.B., and S.-W.Y. N.T. ran and analyzed the lipidomic samples. Proteomic data were acquired by R.N.C., and data were analyzed by A.M.D. miRNA data analyses were performed by A.L.T. and K.W.W. ChIP assay was performed by M.G. and P.C. All BBB modeling were performed by B.M. and D.W.W., and J.W.B., A.M.D., and N.J.H. wrote the manuscript. All authors commented and revised the manuscript.

Competing interests: P.C. is the founding director of the Advanced Science Research Center Neuroscience Initiative (City University of New York).

Data and materials availability: The proteomics data from astrocytic EVs have been deposited to the PRIDE database, accession ID: PXD006087. The miRNA NanoString data have been deposited to Gene Expression Omnibus, accession ID: GSE96609.

injury, we set out to find a soluble mediator for this phenomenon. We found that extracellular vesicles (EVs) shed from astrocytes in response to intracerebral injection of interleukin-1β (IL-1β) rapidly entered into peripheral circulation and promoted the transmigration of leukocytes through modulation of the peripheral acute cytokine response. Bioinformatic analysis of the protein and microRNA cargo of EVs identified peroxisome proliferator–activated receptor α (PPARα) as a primary molecular target of astrocyte-shed EVs. We confirmed in mice that astrocytic EVs promoted the transmigration of leukocytes into the brain by inhibiting PPARα, resulting in the increase of nuclear factor κB (NF-κB) activity that triggered the production of cytokines in liver. These findings expand our understanding of the mechanisms regulating communication between the brain and peripheral immune system and identify astrocytic EVs as a molecular regulator of the immunological response to inflammatory brain damage.

INTRODUCTION

The historic concept that the brain responds to immune challenges independent of the peripheral system has been amended in recent years. The brain is now more accurately described as “immunologically specialized,” owing to the atypical nature of responses to injury that involve bidirectional communication between the brain and peripheral immune system (1, 2). Brain injuries, such as stroke, trauma, and inflammatory lesions, are associated with both an acute injury and secondary damage that involve the infiltration of immune cells, which can continue for weeks to months after injury (3, 4). The infiltration of immune cells into the brain involves the induction of a peripheral acute cytokine response (ACR) that primes leukocytes to transmigrate to the site of brain damage. Although the peripheral ACR to brain damage occurs in multiple peripheral organs, it is strongest in the liver and is associated with induction of inflammatory cytokines, chemokines, and acute-phase proteins that play essential roles in priming leukocytes for transmigration to the site of brain injury (5–10). Despite decades of research, the precise mechanism by which the injured brain instructs the peripheral immune system remains unknown. Resection of the vagus nerve has been shown to block some elements of this communication in a protective fashion after stroke (11). However, data from focal inflammatory lesion studies in sympathectomized and parasympathectomized animals suggest that the communication of brain injury to the peripheral immune system does not require intact nerve fibers (2) but does involve unidentified blood-borne factors that initiate the liver ACR (12). Here, we show that astrocyte-shed extracellular vesicles (EVs) promote leukocyte transmigration through regulation of the ACR to interleukin-1β (IL-1β)–induced inflammatory brain lesion.

RESULTS

Brain neutral sphingomyelin hydrolase 2 and ceramide regulate leukocyte trafficking in response to IL-1β–induced brain injury

The inflammatory cytokine IL-1β is a potent regulator of the inflammatory response to brain injury (4, 8, 10, 13–15). On the basis of evidence that ligation of the IL-1β receptor rapidly activates a neutral sphingomyelin hydrolase (nSMase) (16), we first determined whether this pathway contributed to the influx of leukocytes in response to a focal IL-1β lesion. Intrastriatal injection of IL-1β promoted an influx of $Ly6b^+$ leukocytes to the lesion site that

was reduced in mice expressing a mutated form of nSMase2 (*m-smpd3*; Fig. 1, A and B) (17). Because the *m-smpd3*$^{fro/fro}$ mouse expresses an inactive form of nSMase2 in all tissues, we determined whether inhibition of brain nSMase was sufficient to inhibit leukocyte influx in response to IL-1β. Coadministration of IL-1β with the noncompetitive nSMase2 antagonist GW4869 reduced leukocyte influx, whereas coadministration of IL-1β with the general nSMase antagonist altenusin (known to inhibit multiple isoforms of nSMase) (18) produced near-complete blockade of leukocyte influx (Fig. 1, A and C). Because altenusin also inhibits the protein tyrosine kinase p60$^{c\text{-}Src}$ (19), we administered a selective inhibitor or p60$^{c\text{-}src}$ (PP1) (20) with IL-1β and found no reduction in leukocyte recruitment (fig. S1, A and B). IL-1β rapidly increased long-chain ceramides (C16:0–C20:0; Fig. 1D and fig. S1C) with corresponding decreases in long-chain sphingomyelins (fig. S1D) but had no effect on brain ceramide in *m-smpd3* mice (Fig. 1D and fig. S1C). Injection of IL-1β, but not saline, was associated with a robust microglia and astrocyte activation (Fig. 1E and fig. S1E) and increased brain expression of IL-1β, tumor necrosis factor–α (TNFα), CCL2, and IL-17 (Fig. 1F). Microglial activation and induction of cytokine expression were reduced to levels not different from control by simultaneous administration of IL-1β + altenusin (Fig. 1, E and F, and fig. S1E). Because the Ly6b antibody may also detect macrophage precursors, we confirmed the identification of leukocytes using a second leukocyte specific antisera (MBS) and costained sections with ionized calcium-binding adaptor molecule–1 (IBA-1) to identify microglia. None of the MBS^{+} cells in the striatum of mice administered IL-1β were dual positive for IBA-1 (fig. S1F). These data suggest that IL-1β induction of ceramide, microglia activation, cytokine expression, and leukocyte influx are regulated by brain nSMase.

After inflammatory brain injury, peripheral leukocytes transmigrate to the site of brain injury by a mechanism that is dependent on a peripheral ACR (5, 10). Therefore, we determined whether brain nSMase regulates the ACR in the liver, lung, and spleen, given that these are the three major organ systems implicated in the ACR after brain injury (10, 21, 22). Intrastriatal administration of IL-1β was associated with a rapid induction of the inflammatory cytokines IL-1β, IL-6, TNFα, and the chemoattractant CCL2 in the liver (Fig. 1G), with a similar cytokine induction in the lung (+IL-17; Fig. 1H), and with a less robust response in the spleen (IL-1β and CCL2 only; Fig. 1I). Coinjection of IL-1β + altenusin prevented the ACR in the liver and lung, but not in the spleen (Fig. 1, G to I). Twenty-four hours after striatal IL-1β administration, the liver and lung ACR diminished to control levels with the exception of liver CCL2 (fig. S2, A and B). The spleen ACR response was sustained for at least 24 hours after intrastriatal infusion of IL-1β with a progressive increase in TNFα expression (fig. S2C). Thus, the ACR after inflammatory brain lesion is regulated in the liver by mechanisms dependent on brain nSMase, whereas the ACR in the lung and spleen is partially and entirely independent of brain nSMase, respectively.

Protein and microRNA cargo of astrocyte-shed EVs regulate the peripheral ACR to inflammatory brain lesion

On the basis of data suggesting that ceramide and nSMase regulate the production and release of EVs (23, 24), we reasoned that IL-1β may induce the release of EVs that enter into peripheral circulation to regulate the ACR. Striatal injection of IL-1β resulted in a trend

toward increased circulating EVs in plasma at 2 hours, with significant increases at 24 hours from $1.6 \times 10^{10} \pm 6.6 \times 10^{9}$ in control (not injected) to $5.8 \times 10^{10} \pm 1.0 \times 10^{10}$ in IL-1β–injected mice. Circulating EVs in mice injected with saline were not different from control ($2.3 \times 10^{10} \pm 7.7 \times 10^{9}$; fig. S2, D and E). We isolated EVs from the plasma of mice intrastriatally injected with either saline or IL-1β and infused 3.0×10^{9} EVs (fig. S3, A to D) into the tail veins of recipient mice with a central ACR block produced with administration of IL-1β + altenusin (Fig. 2A). The adoptive transfer of EVs from mice injected with IL-1β induced liver expression of IL-1β, IL-6, TNFα, and CCL2 (Fig. 2B) and restored the transmigration of leukocytes to the site of IL-1β + altenusin injection (Fig. 2, C and D). Twenty-four hours after the adoptive transfer of EVs, the liver ACR returned to basal levels with the exception of CCL2 (fig. S3F). The liver ACR and the recruitment of leukocytes into the striatum after the adoptive transfer of EVs into mice with a central ACR block were indistinguishable from the response produced after a simple intrastriatal administration of IL-1β (compare to Fig. 1, A and G). However, because the brain cytokine response to IL-1β was blocked by altenusin (Fig. 1F), it was not clear how leukocytes targeted the striatum. We found that although the brain cytokine response was blocked by coinjection of IL-1β + altenusin, focal expression of the vascular adhesion protein intercellular adhesion molecule–1 (ICAM-1) was not affected by central inhibition of nSMase (Fig. 2E). EVs isolated from the plasma of mice receiving brain injections of saline, or EVs isolated from the plasma of mice administered with IL-1β but stripped of protein and microRNA (miRNA) content (fig. S3E), did not induce a liver ACR and did not restore the transmigration of leukocytes into brain parenchyma (Fig. 2, B to D). These data suggest that the protein and miRNA cargo of EVs regulate the peripheral ACR and leukocyte response to an inflammatory brain lesion. Leukocytes appear to target vascular adhesion molecules expressed in response to IL-1β, and this expression is independent of nSMase2 activation.

Although an assortment of central nervous system (CNS) cells are capable of shedding EVs (25–28), we focused our efforts on astroglia based on the intimate association of these cells with the blood-brain barrier (BBB) (29) and observations that astrocytes shed far more EVs in response to IL-1β compared with microglia. IL-1β induced a rapid release of EVs from cultured primary astrocytes ($2.17 \times 10^{9} \pm 2.89 \times 10^{8}$/ml EVs were released within 2 hours in response to a medium change with serum removal, and $2.37 \times 10^{9} \pm 2.08 \times 10^{8}$/ml were released in response to IL-1β) that we visualized using the styryl pyridinium dye FM1-43 (Fig. 3A and movie S1). EV release occurred at sites where IL-1β induced a rapid formation of membrane microdomains enriched for ceramide, the ganglioside GM1, and nSMase2 (Fig. 3, A to C). EV release was blocked by pretreatment with an IL-1 receptor antagonist or the nSMase antagonist altenusin (Fig. 3, A to E). IL-1β stimulation in the presence of altenusin resulted in the formation of subcellular vacuoles indicative of multivesicular bodies, but these appeared to not fuse with the plasma membrane (Fig. 3, A to C, far right column). These data are consistent with our previous reports that plasma membrane fusion events involve a regulated production of ceramide by nSMase (30, 31) and with reports that nSMase and ceramide are required for EV biogenesis and release (23, 32). Rapid formation of membrane microdomains and EV release were also observed in astrocytes exposed to TNFα (IL-1β and TNFα are both potent stimulators of nSMase activity) but not in response to IL-10, which has no known association with nSMase (fig. S4, A to C). These data suggest

that IL-1β induced a rapid formation of ceramide-, GM1-, and nSMase2-enriched membrane microdomains located in astrocyte lipid rafts that were the primary sites of EV release.

To determine whether astrocyte-shed EVs were sufficient to promote leukocyte influx in vivo, we injected an adenovirus vector to express a glial fibrillary acidic protein (GFAP)–driven short hairpin RNA (shRNA) to selectively reduce nSMase2 in astrocytes (Fig. 3F). Protein expression of nSMase2 was reduced 3 days after injection of adenovirus (Fig. 3, G and H), and leukocyte influx in response to injection of IL-1β was blocked (Fig 3I and fig. S4D). To further demonstrate that astrocyte EVs were sufficient to promote the transmigration of leukocytes into the brain, we next purified green fluorescent protein (GFP^+) EVs from cultured GFAP-GFP astrocytes (shed in response to IL-1β) and infused 3.0×10^9 EVs or protein and RNA-depleted EVs (Fig. 3J and fig. S4, E and F) into the tail vein of mice with an ACR block produced by coadministration of IL-1β + altenusin into the striatum. Venous-infused GFP^+ EVs were observed in the liver (fig. S4, G and H), were associated with a liver ACR (Fig. 3K), and promoted leukocyte influx into the brain (Fig. 3, L and M) in a manner indistinguishable from animals administered with IL-1β alone (compare with Fig. 1, A to C and G). Infusion of protein and RNA-depleted astrocyte EVs did not induce a liver ACR and did not promote leukocyte influx into brain parenchyma (Fig. 3, K to M). These data suggest that EVs shed from astrocytes in response to IL-1β are sufficient to promote a robust transmigration of leukocytes into the brain.

Astrocyte-shed EVs rapidly cross the BBB and are targeted to peripheral organs

If astrocyte-shed EVs facilitate the recruitment of leukocytes to the site of inflammatory brain lesion, they must efficiently cross the BBB. To address this question, we first used an in vitro Transwell model of the BBB cultured with brain vascular endothelial cells and astrocytes from GFAP-GFP mice. Exposure of the astrocyte side of the bilayer to IL-1β induced a rapid flux of GFP^+ EVs into the luminal side of the model, without any change in barrier permeability (Fig. 4A and fig. S5, A and B). Inhibition of nSMase with altenusin, IL-1 receptor blockade, or physical disruption of membrane microdomains with the cholesterol-chelating agent β-cyclodextrin (33) prevented the luminal flux of EVs (Fig. 4A). Using transmission electron microscopy (TEM), we observed the formation and fusion of multivesicular bodies in astrocytes, endothelial uptake, and release of EVs in IL-1β–stimulated BBB cultures (fig. S5, C to H). Immunogold TEM of GFP in the BBB model (Fig. 4B) and in brain tissues from GFAP-GFP mice injected with IL-1β (Fig. 4C) confirmed in vivo that EVs observed in the cytosol of endothelial cells originated from astrocytes. Immunogold labeling of GFP was not detected in wild-type mice (Fig. 4D). Although IL-1β has previously been shown to not perturb the BBB in adult mice (34), we confirmed the absence of immunoglobulin G (IgG) in brain parenchyma of adult mice injected with IL-1β (fig. S5, I and K). IgG was readily apparent in brain parenchyma of 2-week-old mice injected in the striatum with IL-1β (fig. S5, J and K), consistent with a more permeable BBB in immature mice. These data demonstrate that EVs released from astrocytes can cross endothelial cells and are released into circulation.

We next used GFAP-GFP mice to identify the peripheral targets of astrocyteshed EVs (Fig. 4, E to L). We observed a basal level of GFP^+ EVs in the liver, lung, and spleen that was not

apparent in nontransgenic mice (Fig. 4, E, F, H, I, K, and L), suggesting that there is a constitutive low-level trafficking of EVs from astrocytes into circulation. Two hours after injection of IL-1β into the brain, we observed a three- to fourfold increase in the number of GFP^+ EVs in the liver, lung, and spleen that was not apparent when IL-1β was injected along with altenusin (Fig. 4, E, F, H, I, K, and L). Twenty-four hours after IL-1β injection, there were sharp reductions in the number of GFP^+ EVs in each of these organs compared to the 2-hour peak response (Fig. 4, G, J, and M), presumably reflecting a reduction in release and the processing of incorporated EVs. To confirm that GFP^+ EVs observed in the liver originated from brain astrocytes, we co-infused FM 1-43 (to label brain cells) and IL-1β (to simulate EV release) into the striatum of GFAP–enhanced GFP (EGFP) mice and observed dual-labeled EVs in the liver (Fig. 4N), demonstrating that GFP^+ EVs in the liver originated from brain astrocytes.

Analysis of EV cargo identified peroxisome proliferator–activated receptor α as a subcellular target in the liver that regulates the peripheral immune response to inflammatory brain lesion

To determine the molecular mechanisms by which EVs regulate the peripheral ACR to brain injury, we characterized the protein, lipid, and miRNA content of EVs shed from IL-1β–stimulated astrocytes. EVs released during a 2-hour time frame after IL-1β stimulation were 66.28 ± 23.46 nm in diameter (Fig. 5, A and B); CD63-, TSG101- and flotillin-immunopositive; and actinin-4–, mitofilin-, and β-actin–immunonegative (Fig. 5C). Proteomic analysis of EVs shed from astrocytes in response to IL-1β identified 212 distinct proteins that were largely related to molecular function, catalytic activity, and binding (tables S1 and S2). There were 10 proteins unique to EVs shed in response to IL-1β, 127 proteins unique to constitutively released EVs, and 75 proteins common to both groups. None of the 124 different miRNAs detected were unique to any group, but 23 were enriched twofold or more in EVs shed from IL-1β–stimulated astrocytes (fig. S6B and table S3). Some of the miRNA identified in EVs from other studies were not present in our analyses, including miR-155, miR-146a, and miR-124 (35–37). There are several possible explanations for the differences in the EV miRNA content. There are likely differences in the miRNA content of exosomes released from different cell types in response to the same stimulus. There are likely differences in the miRNA content depending on when the EVs are collected after stimulation, and different stimuli may produce slightly different compositions of miRNA cargo. Because the cargo of EVs is complex, we reasoned that a focus on any protein or miRNA would not likely provide an accurate representation of the function for these signaling complexes. Therefore, we examined the protein and miRNA cargo of EVs and identified peroxisome proliferator–activated receptor α (PPARα) as a likely molecular target of astrocyte EVs shed in response to IL-1β. This pathway was suggested by a protein-mediated positive regulation of HSP90 (a repressor of PPARα) (38), negative regulation in the enzymatic production of adenosine 3′,5′-monophosphate (cAMP) and diacylglycerides [promotes PPARα activity through PKA (cAMP-dependent protein kinase) or PKC (protein kinase C)] (39, 40), and inhibition of Ras by several miRNAs in the let-7 family (Fig. 5E and table S3). Because PPAR actively suppresses cytokine expression through inhibitory effects on nuclear factor κB (NF-κB) (41) and is enriched in tissues that oxidize fatty acids, with highest expression in the liver (42, 43), we conducted immunoprecipitation of chromatin

isolated from liver samples of mice after striatal injection of IL-1β and found increased binding of the NF-κB subunit c-Rel to promoter regions of *CCL2*, *IL-1*β, and *TNF*α, but not to *IL-17*, consistent with the observed liver ACR response (Fig. 5, F to I, and fig. S6, C and D). Together, these data suggest that EVs shed from astrocytes in response to IL-1β may induce a liver ACR through suppression of PPARα. To test this possibility, we administered the PPARα agonist fenofibrate intraperitoneally (known to have low CNS bioavailability) (44) just before striatal IL-1β infusion, showed that fenofibrate blocked NF-κB binding to *CCL2*, *IL-1*β, and *TNF*α promoter regions (Fig. 5, F to I), and prevented leukocyte transmigration into brain parenchyma (Fig. 5, J and K). In mice with an ACR block produced by coadministration of IL-1β + altenusin, we found that intraperitoneal administration of the PPARα antagonist GW6471 reestablished leukocyte recruitment to the site of IL-1β injection (Fig. 5, L and M). These data suggest that EVs shed from astrocytes in response to IL-1β regulate the expression of inflammatory cytokines in liver through suppression of PPARα.

DISCUSSION

Despite considerable evidence that inflammatory brain lesions promote peripheral leukocytosis through the release of soluble mediators from the brain, attempts to identify these factors have been unsuccessful. Here, we provide evidence that the molecular cargo of EVs released from brain astrocytes is sufficient to promote leukocyte recruitment by regulating the peripheral ACR to a focal IL-1β inflammatory lesion. This identification of a soluble mediator fulfills a critical gap in our understanding of how the brain communicates with the peripheral immune system. Although our data show that EVs released from astrocytes are sufficient to induce a peripheral ACR and leukocyte transmigration, it is likely that EVs released from other brain resident cells and/or vascular endothelium play important roles in fine-tuning the immunological response to brain damage. Several recent studies have demonstrated that EVs released into circulation in the setting of glioblastoma multiforme (45), focal cerebral ischemia, traumatic brain injury (46), Parkinson's disease (47), and Alzheimer's disease (48, 49) carry disease-specific cargo. In addition to trafficking from the brain to peripheral circulation, it has been recently shown that hematopoietic cells release EVs that traffic into the brain to deliver functional RNA to neurons (50), and recent data have shown that choroid plexus epithelium cells sense and transmit information about the peripheral inflammatory status to the brain through the release of EVs that are taken up by astrocytes and microglia (36). These findings combined with data presented in this paper suggest that EVs regulate bidirectional communication between the brain and immune system and that differences in cargo may regulate disease-specific biological responses. Unraveling the molecular mechanisms that regulate this long-distance communication will extend our understanding of how the brain and peripheral systems communicate and may open new therapeutic possibilities for the treatment of neuroimmunological disease.

MATERIALS AND METHODS

Animals

Adult (2 to 3 months) male C57BL/6J (the Jackson Laboratory), Smpd3$^{fro/fro}$ (nSmase2-inactive; provided by C. Poirier) (17), and GFAP-EGFP (the Jackson Laboratory) mice were used for these studies. All animal procedures were performed in accordance with the National Institutes of Health guidelines on animal care and were approved by the Johns Hopkins University Institutional Animal Care and Use Committee.

Focal brain injury model

Striatal injections were performed as previously described (4). The striatum was chosen as the injection site because it is an area of brain parenchyma distant from the meninges, in which the inflammatory responses to the cytokines and endotoxin have been well characterized previously, and to avoid involvement of the ventricles or meninges. We were unable to detect increased levels of exogenously administered IL-1 in the blood after focal microinjection of IL-1β into the striatum. Although the striatum is affected in Parkinson's and Huntington's disease, which makes it a clinically relevant site, the focal unilateral inflammation induced by IL-1β does not produce any overt behavioral changes that affect an animal's ability to access food or water or does not induce heightened sensitivity to pain, which can be a feature if the IL-1β is injected more caudally (for example, in the dorsal raphé nucleus). Mice were anesthetized with 3% isoflurane (Baxter) in oxygen (Airgas) and placed in a stereotaxic frame (Stoelting Co.). A small burr hole was drilled in the skull over the left striatum using a dental drill (Fine Science Tools). IL-1β (0.1 ng/3 μl) alone, with altenusin (50 μM), or with GW4869 (10 μM) was injected (total volume of 3 μl) at the rate of 0.5 μl/min via a pulled glass capillary (tip diameter, <50 μm) (51) using the stereotaxic coordinates: Anterior/Posterior, +1; Medial/Lateral, −2; and Dorsal/Ventral, −3. Saline containing the same amount of dimethyl sulfoxide (0.67%per volume) was used as a control. After infusion, the capillary was held in place for 5 min to allow for the solution to diffuse into the tissue. Animals were sacrificed at 2 and 24 hours by an overdose of anesthetic and transcardically perfused with ice-cold saline containing heparin (20 μl/100ml, Sigma-Aldrich). The liver, lung, and spleen were dissected and flash-frozen. Brains were rapidly extracted and flash-frozen or postfixed in 4% paraformaldehyde (PFA), followed by cryoprotection in a 30% sucrose solution and freezing at −80°C.

Astrocyte culture

Primary cortical astrocyte cell cultures were established and maintained using methods similar to those described previously (52). Briefly, primary astrocytes were isolated from the cerebral cortex of postnatal day 1 C57B6J and GFAP-EGFP mice. Cells were mechanically dissociated in Hanks' balanced salt solution and plated in poly-D-lysine culture flasks containing Dulbecco's modified Eagle's medium/F-12 media (Gibco BRL) and 10% fetal bovine serum (FBS) (Gibco BRL). Type 1 astrocytes were purified by the mechanical removal of less adherent cells. Cultures were 98% GFAP$^+$ astrocytes with type I morphology and were used for experiments between 3 to 10 passages.

EV isolation and quantitation

For plasma-derived EVs, blood was collected via cardiac puncture using a heparin-coated syringe (Sigma-Aldrich) and EDTA tubes (BD Biosciences) 2 hours after striatal injections. Blood was immediately centrifuged at 2700*g* for 15 min (20°C) to obtain plasma. Plasma was further centrifuged at 10,000*g* for 15 min (4°C) to generate platelet-free plasma. Plasma-derived EVs were isolated via ultracentrifugation at 100,000*g* for 3 hours (4°C). Pellets containing EVs were washed twice with 5 ml of saline, and the final pellet was resuspended in saline. EV size and quantity were determined using NanoSight as described below. EVs were used for experiments the same day as isolation. For astrocyte-shed EVs, 18 T150 culture flasks of GFAP-EGFP primary astrocytes (~80% confluent) were gently washed 3× with warm phosphate-buffered saline (PBS) to remove endogenous EVs. Astrocyte EV release was stimulated by the addition of fresh EV-free medium containing IL-1β (200 ng/ml, R&D Systems). Medium was collected 2 hours after stimulation, and EVs were isolated by a multistep ultracentrifugation. Medium was centrifuged at 10,000*g* for 15 min (4°C). Supernatant was removed and ultracentrifuged at 100,000*g* for 3 hours (4°C) to isolate EVs. This short stimulation procedure resulted in the release of EVs with a narrow size range and protein markers consistent with exosomes. EV size, distribution, and concentrations were determined using a NS500 NanoSight nanoparticle tracking analysis system (Malvern Instruments). EVs were visualized with scattered light from a 488-nm laser beam onto an optical microscope containing a charge-coupled device video camera. Five exposures of 20 s each were randomly chosen by the software to measure EV size and concentration based on the Stokes-Einstein equation and linear fitting using standard particles with a known diameter. Data were binned and plotted as a continuous histogram.

Depletion of proteins and RNA from EVs

The lipid components from plasma- and astrocyte-derived EVs were isolated using a modified Bligh and Dyer procedure as previously described (53). Using this procedure, RNA localizes to the upper aqueous fraction, lipids localize to the lower chloroform layer, and proteins are precipitated at the interface of the aqueous and organic layer. The chloroform fraction containing a crude lipid extract was dried under a stream of nitrogen and resuspended in saline, and uniform-sized vesicles were created using a mini extruder with 80-nm-pore–sized membrane (Avanti). Liposomes were used on the same day of isolation for experiments.

Adoptive transfer of EVs

EVs were isolated from the plasma of “donor” mice 2 hours after striatal injection of IL-1β (0.1 ng in 3 μl) or saline (3 μl). Plasma EVs (3.0×10^9) were infused into the tail veins of “recipient” mice 2 hours with an ACR block produced by striatal coinjection of IL-1β + nSMase antagonist altenusin (50 μM). Mice were sacrificed 2 or 24 hours after EV infusion. Organs were isolated for biochemical and histological analyses.

Transwell model of the BBB

An in vitro model of the BBB was generated using a previously published method (54) with minor modifications. GFAP-EGFP primary astrocytes were used to visualize EVs (EVs shed

from these cells carry EGFP). BBB function was confirmed by the presence of high transendothelial electrical resistance and by a lack of permeability to fluorogenic-labeled albumin and insulin.

Cytokine expression

RNA was isolated from fresh frozen tissues (10 to 50 mg) using the RNeasy Mini Kit (Qiagen). Total RNA was reverse-transcribed and quantified using previously published methods (55). For quantitative real-time PCR (qRT-PCR), each reaction contained SYBR Green Master Mix (12.5 μl; Life Technologies), diethyl pyrocarbonate H_2O (10.5 μl), forward and reverse primers to CCL2, TNFα, IL-6, IL-1β, IL-17, IL-10, IGFR1, and CXCL1 (0.5 μl each; Sigma-Aldrich), and cDNA (1 μl). Each 96-well plate included a nontemplate control, and samples were analyzed in triplicate on an Applied Biosystems 7300 (Life Technologies). Cycling parameters were as follows: one cycle for 2 min at 50°C, one cycle for 10 min at 95°C, and 40 cycles for 15 s at 95°C and for 1 min at 60°C. The change in threshold cycle (ΔC_t) for each sample was normalized to β-actin, and $\Delta\Delta C_t$ was calculated by comparing ΔC_t for the treatment group to the average ΔC_t of the control group (56).

miRNA expression analysis

RNA was isolated from EVs using the miRNeasy Micro Kit (Qiagen). Small RNAs were tagged on their 3′ end to normalize T_m, according to the manufacturer's instructions (NanoString Techologies). Briefly, small RNAs were bridged with tagged DNA in annealing buffer (94°C for 1 min, 65°C for 2 min, 45°C for 10 min, and hold at 48°C). Polyethylene glycol and ligation buffer were added for 5 min at 48°C, then ligase was added (48°C for 3 min, 47°C for 3 min, 46°C for 3 min, 45°C for 5 min, 65°C for 10 min, and hold at 4°C). To remove excess tags and bridges, we purified samples using a ligation cleanup enzyme (37°C for 120 min, 70°C for 10 min, and hold at 4°C). RNA was further prepped for hybridization by adding water (40 μl), heating the samples to 85°C for 10 min, and then immediately placing them on ice. RNA (5 μl) was hybridized to miRNA Reporter CodeSet master mix (20 μl) at 65°C for 18 hours. Hybridized RNAs were bound to nCounter cartridges and analyzed using an nCounter Digital Analyzer (NanoString).

Chromatin immunoprecipitation

Chromatin immunoprecipitation (ChIP) assays were conducted as previously described (57). Frozen tissue samples (40 mg per immunoprecipitate) were cut into small pieces, incubated with PBS containing 1% formaldehyde at room temperature for 8 min, and quenched with 0.125 M glycine. After rinsing twice with ice-cold PBS containing cOmplete protease inhibitors [Protease Inhibitor Cocktail (PIC); Roche], tissues were collected by centrifugation and disaggregated using a homogenizer (Dounce) in 1 ml of ice-chilled PBS (+PIC). Crosslinked cells were collected and resuspended in lysis buffer [5 mM Pipes (pH 8.0), 85 mM KCl, and 0.5% NP-40 v/v] with PIC. After 30 min incubation with lysis buffer, nuclei were pelleted by centrifugation (10 min at 3000 rpm) and incubated with 300 ml of nuclei lysis buffer [50 mM tris-HCl (pH 8.1), 10 mM EDTA, and 1% SDS] with PIC for 15 min on ice and sonicated using a Bioruptor Sonication System (Diagenode). Lysates were clarified by centrifugation at 10,000 rpm at 4°C for 10 min. The size of DNA in the cleared

chromatin fragments was tested before precipitation to ensure that the majority of fragment size was 200 to 400 base pairs. Immunoprecipitation was performed with 1 μg of c-Rel antibody (sc-70 X, Santa Cruz Biotechnology) and 1 μg of normal rabbit IgG per 1 unit OD260 readings. Two units of chromatin were used per condition. Chromatin was immunoprecipitated using Protein A Dynabeads (Invitrogen) at 4°C overnight. Protein-DNA complexes were washed two times with low-salt ChIP buffer [50 mM tris-HCl (pH 8.0), 150 mM NaCl, 0.5% sodium deoxycholate, 0.1% SDS, 1% NP-40, and 1 mM EDTA], two times with high-salt ChIP buffer [50 mM tris-HCl (pH 8.0), 500mM NaCl, 0.5% sodium deoxycholate, 0.1% SDS, 1% NP-40, and 1 mM EDTA], twice with LiCl buffer [10 mM tris-HCl (pH 8.0), 250mMLiCl, 0.5% sodium deoxycholate, 0.1% SDS, 1% NP-40, and 1 mM EDTA], and one final wash with tris-EDTA buffer [10 mM tris-HCl (pH8) and 1 mM EDTA]. Chromatin was eluted twice from the beads by incubation with 50 μl of elution buffer (50 mM $NaHCO_3$, 1% SDS v/v), heated at 65°C with occasional vortexing for 15 min, and decross-linked at 65°C overnight. Input sample underwent a cross-link reversal. Samples were treated with ribonuclease A and proteinase K according to the manufacturer's specifications. DNA was purified by phenol-chloroform extraction followed by ethanol precipitation. Fold enrichment was calculated using the $2\Delta C_t$ method. The primer sequences of quantitative PCR for ChIP are provided in table S4.

Immunohistochemistry

Coronal brain sections (20 to 40 μm) were prepared using a cryostat microtome (Leica). Endogenous peroxidase activity was quenched using a 1% solution of H_2O_2 in MeOH, and primary antibodies Ly6b (1:1000, AbD Serotec), IBA-1 (1:500, Abcam), ICAM-1 (1:100, Abcam) or MBS antisera to neutrophils (58) were incubated at 4°C overnight. Sections were washed (3× PBS), and the appropriate biotinylated secondary antibody (1:100, Vector Laboratories) was added at room temperature for 2 hours. Staining was visualized using an avadin-biotin complex (1:100 of A and B, Vector Laboratories) and DAB-HCl using a microscope to monitor staining progression. Stereological quantitation was performed using a one-in-five series (200-μm spacing), from the rostral point of bregma −1.22 mm to the caudal point of bregma −2.80 mm as previously described (59). A similar protocol was used to determine BBB integrity, except that no primary antibody was used, and the secondary antibody (targeted toward mouse IgG) was visualized (IgG is not present in brain parenchyma when the BBB is intact).

Immunofluorescence

Astrocytes isolated from C57B6J mice were cultured on glass coverslips and treated with IL-1β (100 ng/ml; Millipore), IL-1β + altenusin (50 μM; Enzo Life Sciences), IL-1β + GW4869 (20 μM; Calbiochem), IL-1β + IL-1 receptor agonist (100 ng/ml), TNFα (100 ng/ml), or IL-10 (100 ng/ml) for 2 to 60 min. Cells were fixed with 4% PFA, and lipid raft membrane microdomains were identified using a cholera toxin subunit B conjugated to Alexa Fluor 555, which binds the ganglioside GM1 (CTB-555, Invitrogen/Molecular Probes) (30, 59). CTB-555–labeled cells were incubated with primary antibodies to ceramide (1:200; Santa Cruz Biotechnology) or nSMase (1:200; Santa Cruz Biotechnology), and the corresponding secondary antibodies were conjugated to Alexa Fluor 488 or Alexa Fluor 546 (1:1000; Invitrogen/Molecular Probes). Fluorescence was imaged with a 100×

objective by optical sectioning using structured illumination (Carl Zeiss Inc.). All images for quantification were taken with identical settings and performed on a single plane of focus through the brightest point. Colocalization was confirmed by three-dimensional reconfiguration of *z*-stack images using orthogonal views as previously described (31).

Localization of astrocyte-shed exosomes in peripheral tissues

EVs released from astrocytes of GFAP-EGFP mice were visualized by fluorescence imaging of $EGFP^+$ puncta in liver, spleen, and lung tissue sections. Tissues were postfixed in 4% PFA and cryoprotected in 30% sucrose, and 20-μm sections were cut using a cryostat microtome (Leica). Nonspecific binding was blocked with 5% normal goat serum plus 5% normal horse serum in tris-buffered saline (TBS) containing 0.1% Triton X-100 (Fisher Scientific). EGFP was enhanced by incubating sections with anti-GFP rabbit sera (1:500; Invitrogen) at 4°C overnight, followed by incubation with a secondary antibody conjugated to Alexa Fluor 488 (1:1000; Invitrogen). Cells were visualized with F-actin (1:100; Abcam), and nuclei were stained with DAPI as previously described (60). Imaging was performed with 40× and 100× objectives using optical sectioning by structured illumination (Carl Zeiss Inc.).

Western blotting

Proteins were resolved by 10% SDS–polyacrylamide gel electrophoresis and transferred to polyvinylidene difluoride membranes (Bio-Rad). Nonspecific binding sites were blocked with 5% (w/v) milk in TBS containing 0.1% Tween 20 (TBS-T). After blocking, blots were incubated overnight with the primary polyclonal antibody flotillin 1 (1:1000; Abcam), CD63 (1:200; Santa Cruz Biotechnology), TSG101 (1:1000; BD Biosciences), actinin-4 (1:1000; Gentex), microfilin (1:5000; Thermo Fisher Scientific), nSMase2 (1:500; Santa Cruz Biotechnology), transferrin receptor (1:1000; Invitrogen), and β-actin (1:5000; Sigma-Aldrich). After washes with TBS-T, blots were incubated for 2 hours with the appropriate IgG horseradish peroxidase–linked secondary antibody (1:1000; Cell Signaling Technology) and developed by enhanced chemiluminescence. Image analysis was performed using a G:BOX imaging system (Syngene).

Electron microscopy

For the negative stain, glow-discharged 400 mesh copper/carbon-coated grids (Electron Microscopy Sciences) were placed on 5 to 10 μl of liquid sample for 1 min and then briefly washed with drops of distilled water. The grids were stained in 2% uranyl acetate (Electron Microscopy Sciences) for 1 min and blotted dry on Whatman filter paper (Sigma-Aldrich). Imaging was performed on a Libra 120 electron microscope (Zeiss) at an acceleration voltage of 120 kV using a Veleta camera (Olympus).

For the immunogold electron microscopy, thin sections of Epon-embedded tissue (Electron Microscopy Sciences) (61) were placed on nickel grids (Electron Microscopy Sciences) and etched in 3% sodium (meta)periodate (Electron Microscopy Sciences) two times for 30 min each and then washed with double-distilled H_2O. Sections were incubated in PBS containing 10% FBS for 30 min and incubated overnight in GFP antisera (Invitrogen; 1:50 at 4°C). After several washes in PBS, grids were incubated at room temperature in goat anti-rabbit secondary (Jackson ImmunoResearch; 1:20). Grids were washed in PBS and fixed briefly in

2% glutaraldehyde (Sigma-Aldrich). Staining was performed using uranyl acetate, followed by lead citrate. Grids were viewed on a Libra 120 electron microscope (Zeiss) using a Veleta camera (Olympus).

Ceramide analysis

Ceramides were quantified by mass spectrometry as previously described (62), with slight modifications. A crude lipid extraction was prepared from tissues using a variation of the Bligh and Dyer procedure (63), with ceramide d18:0/12:0 (Avanti Polar Lipids) included as an internal standard. The organic layer containing a crude lipid extract was dried in a nitrogen evaporator (Organomation) and suspended in MeOH before analysis. Chromatographic separations were conducted using an ultrafast liquid chromatography system (Shimadzu) coupled to a C18 reversed-phase column (Phenomenex). Eluted samples were injected into an API 3000 triple quadrupole mass spectrometer (AB Sciex), in which individual ceramide species (C16:0–C26:1) were detected by multiple reaction monitoring. Eight-point calibration curves (0.1 to 1000 ng/ml) were constructed by plotting the area under the curve for each calibration standard (d18:1/C16:0, d18:1/C18:0, d18:1/C20:0, d18:1/C22:0, and d18:1/ C24:0) normalized to the internal standard. Correlation coefficients (R^2) obtained were >0.999. Ceramide concentrations were calculated by fitting the identified ceramide species to these standard curves based on acyl chain length. Instrument control and quantitation of spectral data were performed using Analyst 1.4.2 and MultiQuant software (AB Sciex).

Proteomics

EVs isolated from astrocytes were digested with trypsin overnight and analyzed by liquid chromatography–tandem mass spectrometry (LC-MS/MS) using LTQ Orbitrap Velos MS (Thermo Fisher Scientific) interfaced with nanoACQUITY (Waters), as previously described (64), with precursor and fragment ions analyzed at resolution of 30,000 and 15,000, respectively. Proteins were identified from the MS/MS spectra extracted in Proteome Discoverer (version 1.4; Thermo Fisher Scientific) interfaced with Mascot (version 2.5; Matrix Science) to search the SwissProt_2014_07 database with the following criteria: *Mus musculus* species; precursor and fragment ions mass tolerance of 0.050 Da and 15 parts per million, respectively; fixed modification cysteine carbamidomethylation; and variable modifications of asparagine and glutamine deamination, methionine oxidation, and serine, threonine, and tyrosine phosphorylation. Protein identifications were confirmed using Scaffold version 4.4.1 (Proteome Software) at >91% probability with <1% false discovery rate with at least two peptide sequences per protein. The gene ontology classifications were performed in Scaffold version 4.4.1 (Proteome Software). Proteins were classified using the Protein Analysis Through Evolutionary Relationship (PANTHER) tool (65).

In vivo gene silencing of nSMase2 in astrocytes

A GFAP-promoted shRNA targeting nSMase2 and coexpressing mCherry in an adeno-associated viral vector (serotype2) was designed using the previously published small interfering RNA sequence (66) and manufactured commercially (SignaGen). A scrabbled shRNA nSMase2 coexpressing mCherry in an adeno-associated viral vector (SignaGen) was used as a negative control. Viral vectors (5×10^9 particles in 0.5 μl) were injected into the

striatum using a pulled glass capillary as described above. Intrastriatal injections were performed 72 hours after administration of viral vectors. Vector expression was confirmed by mCherry staining of brain slices, and knockdown of nSMase2 was confirmed by Western blotting. The animals were sacrificed 24 hours after injection of IL-1β. Organs were isolated for biochemical and histological analysis.

Pathway discovery and biological validation

Putative molecular pathways regulated by EV cargo were identified using Ingenuity Pathway Analysis (IPA) (Qiagen). Proteomic and miRNA data were converted to fold change and uploaded to the IPA server (Qiagen). A core analysis (IPAv23814503) was performed using all data sources available in the software. Resultant canonical pathways and interaction networks were examined, and pathways with relevance to the regulation of inflammation were considered for biological validation. The involvement of a central regulator in the identified pathway (PPARα) was confirmed in vivo by intraperitoneal injection of small-molecule drugs to target PPARα that included the agonist fenofibrate (10 mg/kg; Sigma-Aldrich) and the antagonist GW6471 (20 mg/kg; Tocris Bioscience) after striatal administrations of IL-1β or IL-1β + altenusin as described. Mice were scarified after 2 hours for biochemical and histological analyses and after 24 hours for leukocyte transmigration.

Statistical analyses

Group differences were determined by ANOVA with Tukey post hoc comparisons. Hierarchal cluster analysis was conducted using $\log_2$ values of normalized median counts. Heat maps and clustering were generated using “pheatmap” (version 0.7.7; R package version 3.1.1) (67).

Supplementary Material

Refer to Web version on PubMed Central for supplementary material.

Acknowledgments

We thank C. Cooke at the Johns Hopkins School of Medicine Department of Neurology for acquisition of EM images used in this study. **Funding:** These studies were supported by NIH grants R01MH077542, R01MH096636, R03MH103985, and PO1MH075673 to N.J.H.; and R01MH075679, R01MH090958, and R21MH102112 to J.W.B.

References

1. Ransohoff RM, Kivisäkk P, Kidd G. Three or more routes for leukocyte migration into the central nervous system. Nat. Rev. Immunol. 2003; 3:569–581. [PubMed: 12876559]
2. Anthony DC, Couch Y, Losey P, Evans MC. The systemic response to brain injury and disease. Brain Behav. Immun. 2012; 26:534–540. [PubMed: 22085588]
3. Smith DH, Chen X-H, Pierce JE, Wolf JA, Trojanowski JQ, Graham DI, McIntosh TK. Progressive atrophy and neuron death for one year following brain trauma in the rat. J Neurotrauma. 1997; 14:715–727. [PubMed: 9383090]
4. Wilcockson DC, Campbell SJ, Anthony DC, Perry VH. The systemic and local acute phase response following acute brain injury. J Cereb. Blood Flow Metab. 2002; 22:318–326. [PubMed: 11891437]
5. Campbell SJ, Zahid I, Losey P, Law S, Jiang Y, Bilgen M, van Rooijen N, Morsali D, Davis AEM, Anthony DC. Liver Kupffer cells control the magnitude of the inflammatory response in the injured brain and spinal cord. Neuropharmacology. 2008; 55:780–787. [PubMed: 18674548]

6. Pepys M, Baltz ML. Acute phase proteins with special reference to C-reactive protein and related proteins (pentaxins) and serum amyloid A protein. Adv. Immunol. 1983; 34:141–212. [PubMed: 6356809]
7. Zahedi K, Whitehead AS. Acute phase induction of mouse serum amyloid P component. Correlation with other parameters of inflammation. J Immunol. 1989; 143:2880–2886. [PubMed: 2809211]
8. Campbell SJ, Hughes PM, Iredale JP, Wilcockson DC, Waters S, Docagne F, Perry VH, Anthony DC. CINC-1 is an acute-phase protein induced by focal brain injury causing leukocyte mobilization and liver injury. FASEB J. 2003; 17:1168–1170. [PubMed: 12709409]
9. Clausen F, Hånell A, Björk M, Hillered L, Mir AK, Gram H, Marklund N. Neutralization of interleukin-1β modifies the inflammatory response and improves histological and cognitive outcome following traumatic brain injury in mice. Eur. J. Neurosci. 2009; 30:385–396. [PubMed: 19614750]
10. Campbell SJ, Anthony DC, Oakley F, Carlsen H, Elsharkawy AM, Blomhoff R, Mann DA. Hepatic nuclear factor κB regulates neutrophil recruitment to the injured brain. J Neuropathol. Exp. Neurol. 2008; 67:223–230. [PubMed: 18344913]
11. Ottani A, Giuliani D, Mioni C, Galantucci M, Minutoli L, Bitto A, Altavilla D, Zaffe D, Botticelli AR, Squadrito F, Guarini S. Vagus nerve mediates the protective effects of melanocortins against cerebral and systemic damage after ischemic stroke. J Cereb. Blood Flow Metab. 2008; 29:512–523. [PubMed: 19018269]
12. Jiang Y, Deacon R, Anthony DC, Campbell SJ. Inhibition of peripheral TNF can block the malaise associated with CNS inflammatory diseases. Neurobiol. Dis. 2008; 32:125–132. [PubMed: 18672064]
13. Campbell SJ, Deacon RMJ, Jiang Y, Ferrari C, Pitossi FJ, Anthony DC. Overexpression of IL-1β by adenoviral-mediated gene transfer in the rat brain causes a prolonged hepatic chemokine response, axonal injury and the suppression of spontaneous behaviour. Neurobiol. Dis. 2007; 27:151–163. [PubMed: 17580116]
14. Brough D, Tyrrell PJ, Allan SM. Regulation of interleukin-1 in acute brain injury. Trends Pharmacol. Sci. 2011; 32:617–622. [PubMed: 21788085]
15. Mrak RE, Griffin WST. Interleukin-1, neuroinflammation, and Alzheimer's disease. Neurobiol. Aging. 2001; 22:903–908. [PubMed: 11754997]
16. Mathias S, Younes A, Kan C-C, Orlow I, Joseph C, Kolesnick RN. Activation of the sphingomyelin signaling pathway in intact EL4 cells and in a cell-free system by IL-1 beta. Science. 1993; 259:519–522. [PubMed: 8424175]
17. Aubin I, Adams CP, Opsahl S, Septier D, Bishop CE, Auge N, Salvayre R, Negre-Salvayre A, Goldberg M, Guénet J-L, Poirier C. A deletion in the gene encoding sphingomyelin phosphodiesterase 3 (*Smpd3*) results in osteogenesis and dentinogenesis imperfecta in the mouse. Nat. Genet. 2005; 37:803–805. [PubMed: 16025116]
18. Uchida R, Tomoda H, Dong Y, Omura S. Alutenusin, a specific neutral sphingomyelinase inhibitor, produced by *Penicillium* sp. FO-7436. J Antibiot. 1999; 52:572–574. [PubMed: 10470682]
19. Oyama M, Xu Z, Lee K-H, Spitzer TD, Kitrinos P, McDonald OB, Jones RR, Garvey EP. Fungal metabolites as potent protein kinase inhibitors: Identification of a novel metabolite and novel activities of known metabolites. Lett. Drug Des. Discov. 2004; 1:24–29.
20. Waltenberger J, Uecker A, Kroll J, Frank H, Mayr U, Bjorge JD, Fujita D, Gazit A, Hombach V, Levitzki A, Böhmer F-D. A dual inhibitor of platelet-derived growth factor β-receptor and Src kinase activity potently interferes with motogenic and mitogenic responses to PDGF in vascular smooth muscle cells. A novel candidate for prevention of vascular remodeling. Circ. Res. 1999; 85:12–22. [PubMed: 10400906]
21. Engel O, Akyüz L, da Costa Goncalves AC, Winek K, Dames C, Thielke M, Herold S, Böttcher C, Priller J, Volk HD, Dirnagl U, Meisel C, Meisel A. Cholinergic pathway suppresses pulmonary innate immunity facilitating pneumonia after stroke. Stroke. 2015; 46:3232–3240. [PubMed: 26451017]
22. Offner H, Vandenbark AA, Hurn PD. Effect of experimental stroke on peripheral immunity: CNS ischemia induces profound immunosuppression. Neuroscience. 2009; 158:1098–1111. [PubMed: 18597949]

23. Trajkovic K, Hsu C, Chiantia S, Rajendran L, Wenzel D, Wieland F, Schwille P, Brügger B, Simons M. Ceramide triggers budding of exosome vesicles into multivesicular endosomes. Science. 2008; 319:1244–1247. [PubMed: 18309083]
24. Guo BB, Bellingham SA, Hill AF. The neutral sphingomyelinase pathway regulates packaging of the prion protein into exosomes. J Biol. Chem. 2015; 290:3455–3467. [PubMed: 25505180]
25. Lachenal G, Pernet-Gallay K, Chivet M, Hemming FJ, Belly A, Bodon G, Blot B, Haase G, Goldberg Y, Sadoul R. Release of exosomes from differentiated neurons and its regulation by synaptic glutamatergic activity. Mol. Cell. Neurosci. 2011; 46:409–418. [PubMed: 21111824]
26. Potolicchio I, Carven GJ, Xu X, Stipp C, Riese RJ, Stern LJ, Santambrogio L. Proteomic analysis of microglia-derived exosomes: Metabolic role of the aminopeptidase CD13 in neuropeptide catabolism. J Immunol. 2005; 175:2237–2243. [PubMed: 16081791]
27. Guescini M, Genedani S, Stocchi V, Agnati LF. Astrocytes and glioblastoma cells release exosomes carrying mtDNA. J Neural Transm. 2010; 117:1–4. [PubMed: 19680595]
28. Krämer-Albers E-M, Bretz N, Tenzer S, Winterstein C, Möbius W, Berger H, Nave K-A, Schild H, Trotter J. Oligodendrocytes secrete exosomes containing major myelin and stress-protective proteins: Trophic support for axons? Proteomics: Clin. Appl. 2007; 1:1446–1461. [PubMed: 21136642]
29. Sofroniew MV, Vinters HV. Astrocytes: Biology and pathology. Acta Neuropathol. 2010; 119:7–35. [PubMed: 20012068]
30. Wheeler D, Knapp E, Bandaru VVR, Wang Y, Knorr D, Poirier C, Mattson MP, Geiger JD, Haughey NJ. Tumor necrosis factor-α-induced neutral sphingomyelinase-2 modulates synaptic plasticity by controlling the membrane insertion of NMDA receptors. J Neurochem. 2009; 109:1237–1249. [PubMed: 19476542]
31. Xu H, Bae M, Tovar-y-Romo LB, Patel N, Bandaru VVR, Pomerantz D, Steiner JP, Haughey NJ. The human immunodeficiency virus coat protein gp120 promotes forward trafficking and surface clustering of NMDA receptors in membrane microdomains. J Neurosci. 2011; 31:17074–17090. [PubMed: 22114277]
32. Wang G, Dinkins M, He Q, Zhu G, Poirier C, Campbell A, Mayer-Proschel M, Bieberich E. Astrocytes secrete exosomes enriched with proapoptotic ceramide and prostate apoptosis response 4 (PAR-4): Potential mechanism of apoptosis induction in Alzheimer disease (AD). J Biol. Chem. 2012; 287:21384–21395. [PubMed: 22532571]
33. Wadia JS, Stan RV, Dowdy SF. Transducible TAT-HA fusogenic peptide enhances escape of TAT-fusion proteins after lipid raft macropinocytosis. Nat. Med. 2004; 10:310–315. [PubMed: 14770178]
34. Anthony D, Dempster R, Fearn S, Clements J, Wells G, Perry VH, Walker K. CXC chemokines generate age-related increases in neutrophil-mediated brain inflammation and blood–brain barrier breakdown. Curr. Biol. 1998; 8:923–927. [PubMed: 9707404]
35. Alexander M, Hu R, Runtsch MC, Kagele DA, Mosbruger TL, Tolmachova T, Seabra MC, Round JL, Ward DM, O'Connell RM. Exosome-delivered microRNAs modulate the inflammatory response to endotoxin. Nat. Commun. 2015; 6:7321. [PubMed: 26084661]
36. Balusu S, Van Wonterghem E, De Rycke R, Raemdonck K, Stremersch S, Gevaert K, Brkic M, Demeestere D, Vanhooren V, Hendrix A, Libert C, Vandenbroucke RE. Identification of a novel mechanism of blood–brain communication during peripheral inflammation via choroid plexus-derived extracellular vesicles. EMBO Mol. Med. 2016; 8:1162–1183. [PubMed: 27596437]
37. Ji Q, Ji Y, Peng J, Zhou X, Chen X, Zhao H, Xu T, Chen L, Xu Y. Increased brain-specific MiR-9 and MiR-124 in the serum exosomes of acute ischemic stroke patients. PLOS ONE. 2016; 11:e0163645. [PubMed: 27661079]
38. Sumanasekera WK, Tien ES, Davis JW II, Turpey R, Perdew GH, Vanden Heuvel JP. Heat shock protein-90 (Hsp90) acts as a repressor of peroxisome proliferator-activated receptor-α (PPARα) and PPARβ activity. Biochemistry. 2003; 42:10726–10735. [PubMed: 12962497]
39. Lazennec G, Canaple L, Saugy D, Wahli W. Activation of peroxisome proliferator-activated receptors (PPARs) by their ligands and protein kinase A activators. Mol. Endocrinol. 2000; 14:1962–1975. [PubMed: 11117527]

40. Blanquart C, Mansouri R, Paumelle R, Fruchart J-C, Staels B, Glineur C. The protein kinase C signaling pathway regulates a molecular switch between transactivation and transrepression activity of the peroxisome proliferator-activated receptor α. Mol. Endocrinol. 2004; 18:1906–1918. [PubMed: 15131257]
41. Staels B, Koenig W, Habib A, Merval R, Lebret M, Torra IP, Delerive P, Fadel A, Chinetti G, Fruchart J-C, Najib J, Maclouf J, Tedgui A. Activation of human aortic smooth-muscle cells is inhibited by PPARα but not by PPARγ activators. Nature. 1998; 393:790–793. [PubMed: 9655393]
42. Kliewer SA, Forman BM, Blumberg B, Ong ES, Borgmeyer U, Mangelsdorf DJ, Umesono K, Evans RM. Differential expression and activation of a family of murine peroxisome proliferator-activated receptors. Proc. Natl. Acad. Sci. U.S.A. 1994; 91:7355–7359. [PubMed: 8041794]
43. Vega RB, Huss JM, Kelly DP. The coactivator PGC-1 cooperates with peroxisome proliferator-activated receptor α in transcriptional control of nuclear genes encoding mitochondrial fatty acid oxidation enzymes. Mol. Cell. Biol. 2000; 20:1868–1876. [PubMed: 10669761]
44. Deplanque D, Gelé P, Pétrault O, Six I, Furman C, Bouly M, Nion S, Dupuis B, Leys D, Fruchart J-C, Cecchelli R, Staels B, Duriez P, Bordet R. Peroxisome proliferator-activated receptor-α activation as a mechanism of preventive neuroprotection induced by chronic fenofibrate treatment. J Neurosci. 2003; 23:6264–6271. [PubMed: 12867511]
45. Shao H, Chung J, Lee K, Balaj L, Min C, Carter BS, Hochberg FH, Breakefield XO, Lee H, Weissleder R. Chip-based analysis of exosomal mRNA mediating drug resistance in glioblastoma. Nat. Commun. 2015; 6:6999. [PubMed: 25959588]
46. Andrews AM, Lutton EM, Merkel SF, Razmpour R, Ramirez SH. Mechanical injury induces brain endothelial-derived microvesicle release: Implications for cerebral vascular injury during traumatic brain injury. Front. Cell. Neurosci. 2016; 10:43. [PubMed: 26973460]
47. Lööv C, Scherzer CR, Hyman BT, Breakefield XO, Ingelsson M. α-synuclein in extracellular vesicles: Functional implications and diagnostic opportunities. Cell. Mol. Neurobiol. 2016; 36:437–448. [PubMed: 26993503]
48. Kapogiannis D, Boxer A, Schwartz JB, Abner EL, Biragyn A, Masharani U, Frassetto L, Petersen RC, Miller BL, Goetzl EJ. Dysfunctionally phosphorylated type 1 insulin receptor substrate in neural-derived blood exosomes of preclinical Alzheimer's disease. FASEB J. 2015; 29:589–596. [PubMed: 25342129]
49. Fiandaca MS, Kapogiannis D, Mapstone M, Boxer A, Eitan E, Schwartz JB, Abner EL, Petersen RC, Federoff HJ, Miller BL, Goetzl EJ. Identification of preclinical Alzheimer's disease by a profile of pathogenic proteins in neurally derived blood exosomes: A case-control study. Alzheimer's Dementia. 2015; 11:600–607.e1.
50. Ridder K, Keller S, Dams M, Rupp A-K, Schlaudraff J, Del Turco D, Starmann J, Macas J, Karpova D, Devraj K, Depboylu C, Landfried B, Arnold B, Plate KH, Hoglinger G, Sültmann H, Altevogt P, Momma S. Extracellular vesicle-mediated transfer of genetic information between the hematopoietic system and the brain in response to inflammation. PLOS Biol. 2014; 12:e1001874. [PubMed: 24893313]
51. McCluskey L, Campbell S, Anthony D, Allan SM. Inflammatory responses in the rat brain in response to different methods of intra-cerebral administration. J Neuroimmunol. 2008; 194:27–33. [PubMed: 18191461]
52. Haughey NJ, Mattson MP. Alzheimer's amyloid β-peptide enhances ATP/gap junction-mediated calcium-wave propagation in astrocytes. Neuromolecular Med. 2003; 3:173–180. [PubMed: 12835512]
53. Haughey NJ, Cutler RG, Tamara A, McArthur JC, Vargas DL, Pardo CA, Turchan J, Nath A, Mattson MP. Perturbation of sphingolipid metabolism and ceramide production in HIV-dementia. Ann. Neurol. 2004; 55:257–267. [PubMed: 14755730]
54. Williams DW, Anastos K, Morgello S, Berman JW. JAM-A and ALCAM are therapeutic targets to inhibit diapedesis across the BBB of $CD14^+$ $CD16^+$ monocytes in HIV-infected individuals. J Leukoc. Biol. 2015; 97:401–412. [PubMed: 25420915]
55. Westberry JM, Trout AL, Wilson ME. Epigenetic regulation of estrogen receptor α gene expression in the mouse cortex during early postnatal development. Endocrinology. 2010; 151:731–740. [PubMed: 19966177]

56. Livak KJ, Schmittgen TD. Analysis of relative gene expression data using real-time quantitative PCR and the $2^{-\Delta\Delta C}{}_{T}$ method. Methods. 2001; 25:402–408. [PubMed: 11846609]
57. Swiss VA, Nguyen T, Dugas J, Ibrahim A, Barres B, Androulakis IP, Casaccia P. Identification of a gene regulatory network necessary for the initiation of oligodendrocyte differentiation. PLOS ONE. 2011; 6:e18088. [PubMed: 21490970]
58. Bernardes-Silva M, Anthony DC, Issekutz AC, Perry VH. Recruitment of neutrophils across the blood–brain barrier: The role of E- and P-selectins. J Cereb. Blood Flow Metab. 2001; 21:1115–1124. [PubMed: 11524616]
59. Chen X, Hui L, Geiger NH, Haughey NJ, Geiger JD. Endolysosome involvement in HIV-1 transactivator protein-induced neuronal amyloid beta production. Neurobiol. Aging. 2013; 34:2370–2378. [PubMed: 23673310]
60. Tovar-y-Romo L, Kolson D, Bandaru V, Drewes J, Graham D, Haughey N. Adenosine triphosphate released from HIV-infected macrophages regulates glutamatergic tone and dendritic spine density on neurons. J Neuroimmune Pharmacol. 2013; 8:998–1009. [PubMed: 23686368]
61. Craig EL, Frajola WJ, Greider MH. An embedding technique for electron microscopy using Epon 812. J Cell Biol. 1962; 12:190–194. [PubMed: 13881958]
62. Bandaru VVR, Mielke MM, Sacktor N, McArthur JC, Grant I, Letendre S, Chang L, Wojna V, Pardo C, Calabresi P, Munsaka S, Haughey NJ. A lipid storage–like disorder contributes to cognitive decline in HIV-infected subjects. Neurology. 2013; 81:1492–1499. [PubMed: 24027056]
63. Bligh EG, Dyer WJ. A rapid method of total lipid extraction and purification. Can. J. Biochem. Physiol. 1959; 37:911–917. [PubMed: 13671378]
64. Kumar A, Baycin-Hizal D, Wolozny D, Pedersen LE, Lewis NE, Heffner K, Chaerkady R, Cole RN, Shiloach J, Zhang H, Bowen MA, Betenbaugh MJ. Elucidation of the CHO Super-Ome (CHO-SO) by proteoinformatics. J Proteome Res. 2015; 14:4687–4703. [PubMed: 26418914]
65. Mi H, Poudel S, Muruganujan A, Casagrande JT, Thomas PD. PANTHER version 10: Expanded protein families and functions, and analysis tools. Nucleic Acids Res. 2016; 44:D336–D342. [PubMed: 26578592]
66. Marchesini N, Osta W, Bielawski J, Luberto C, Obeid LM, Hannun YA. Role for mammalian neutral sphingomyelinase 2 in confluence-induced growth arrest of MCF7 cells. J Biol. Chem. 2004; 279:25101–25111. [PubMed: 15051724]
67. Kolde R. pheatmap: Pretty heatmaps. R package version 61. 2012

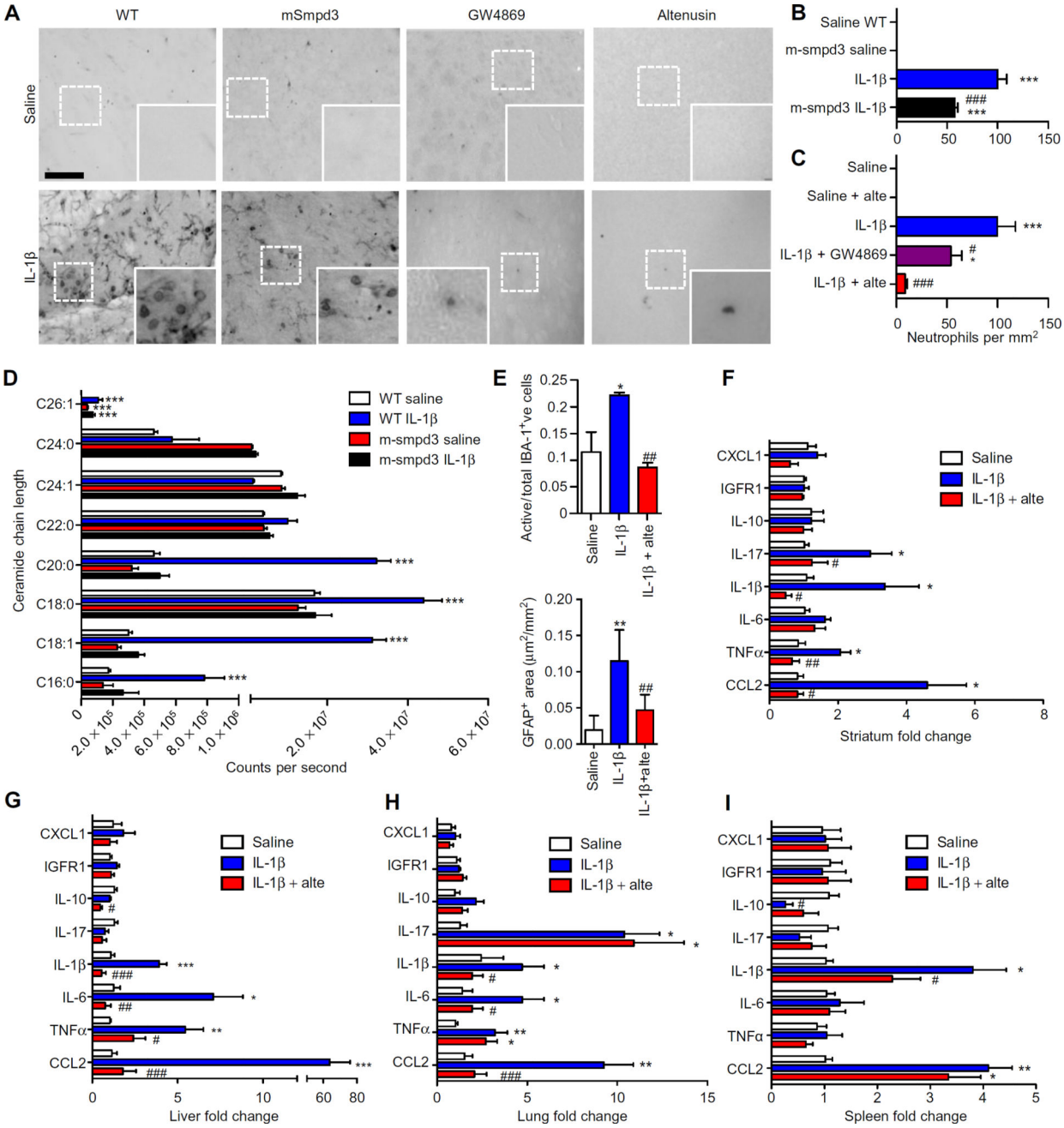

Fig. 1. Brain nSMase regulates the peripheral ACR and leukocyte transmigration after central administration of IL-1β

(**A**) Representative photomicrographs of Ly6b^{+} cells in the striatum of wild-type (WT) or mSmpd3 mice 24 hours after injection of saline or IL-1β (0.1 ng in 3 μl) and in WT mice after coinjection with IL-1β + GW4869 (20 μM) or altenusin (alte; 50 μM). Insets: Magnification of the indicated regions. Scale bar, 250 μm. (**B** and **C**) Stereological quantitation of leukocytes for the indicated conditions. (**D**) Quantitative mass spectrometry of long-chain ceramides in WT mice and mice expressing a deletion mutation in mSmpd3 2 hours after striatal injection of IL-1β or saline. (**E**) Stereological quantitation of activated

IBA-1$^+$ microglia and GFAP$^+$ astrocytes in the striatum of WT mice after striatal injection of IL-1β or IL-1β + altenusin. (**F**) Striatum cytokine expression in WT mice 2 hours after striatal injection of IL-1β or IL-1β + altenusin. (**G** to **I**) Cytokine expression in the liver (G), lung (H), and spleen (I) measured 2 hours after intrastriatal injection of IL-1β or IL-1β + altenusin. Data are means ± SEM of $n = 4$ to 5 mice per condition for ceramide and polymerase chain reaction (PCR) and $n = 3$ mice per condition for leukocyte staining. $^*P < 0.05$, $^{**}P < 0.01$, $^{***}P < 0.001$ compared to control; $^{\#}P < 0.05$, $^{\#\#}P < 0.01$, $^{\#\#\#}P < 0.001$ compared to IL-1β.

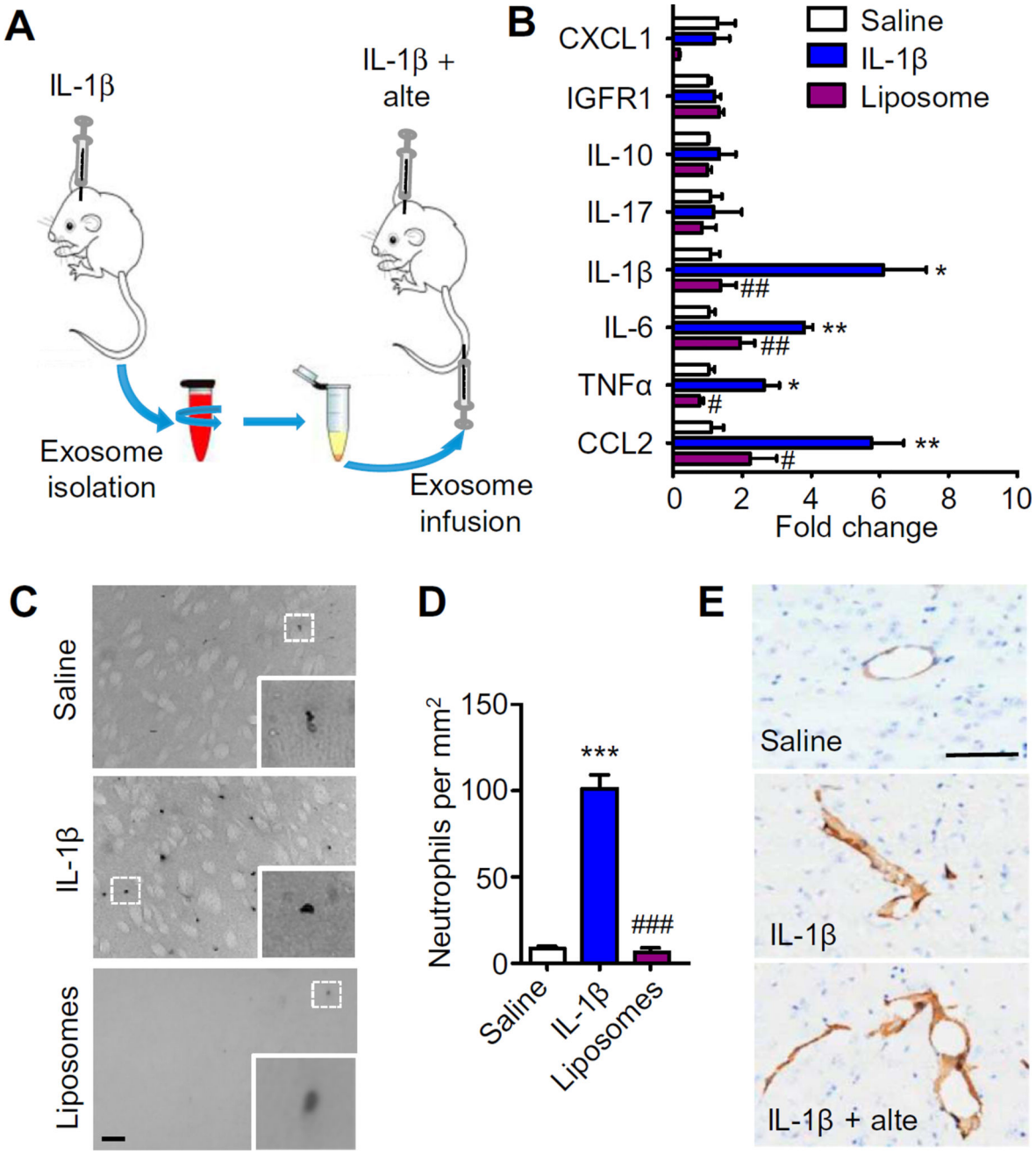

Fig. 2. EVs adoptively transfer an acute peripheral cytokine response

(**A**) Pictorial representation of EV adoptive transfer experiments. EVs were harvested from the plasma of donor mice 2 hours after intrastriatal administration of IL-1β or saline. EVs (3.0×10^9) were then infused into the tail veins of recipient mice that also had intrastriatal injection of IL-1β (0.1 ng in 3 μl) and altenusin (50 μM). As an additional control, recipient mice were infused with EVs depleted of protein and RNA (reconstituted liposomes were 80 nm). (**B**) qRT-PCR data of liver cytokine expression 2 hours after infusions of EVs from donor mice into recipient mice. (**C** and **D**) Representative photomicrographs (C) and stereological quantitation (D) of $Ly6b^+$ leukocytes in the striatum 24 hours after venous

infusion of EVs or liposomes. (**E**) Representative photomicrographs of ICAM-1 staining in the striatum of mice injected with saline, IL-1β, or IL-1β + altenusin. Data are means ± SEM of $n = 4$ to 5 mice per condition for PCR and $n = 3$ mice per condition for leukocyte quantitation. $^{*}P < 0.05$, $^{**}P < 0.01$, $^{***}P < 0.001$ compared to saline; $^{\#}P < 0.05$, $^{\#\#}P < 0.01$, $^{\#\#\#}P < 0.001$ compared to IL-1β. Analysis of variance (ANOVA) with Tukey post hoc comparisons.

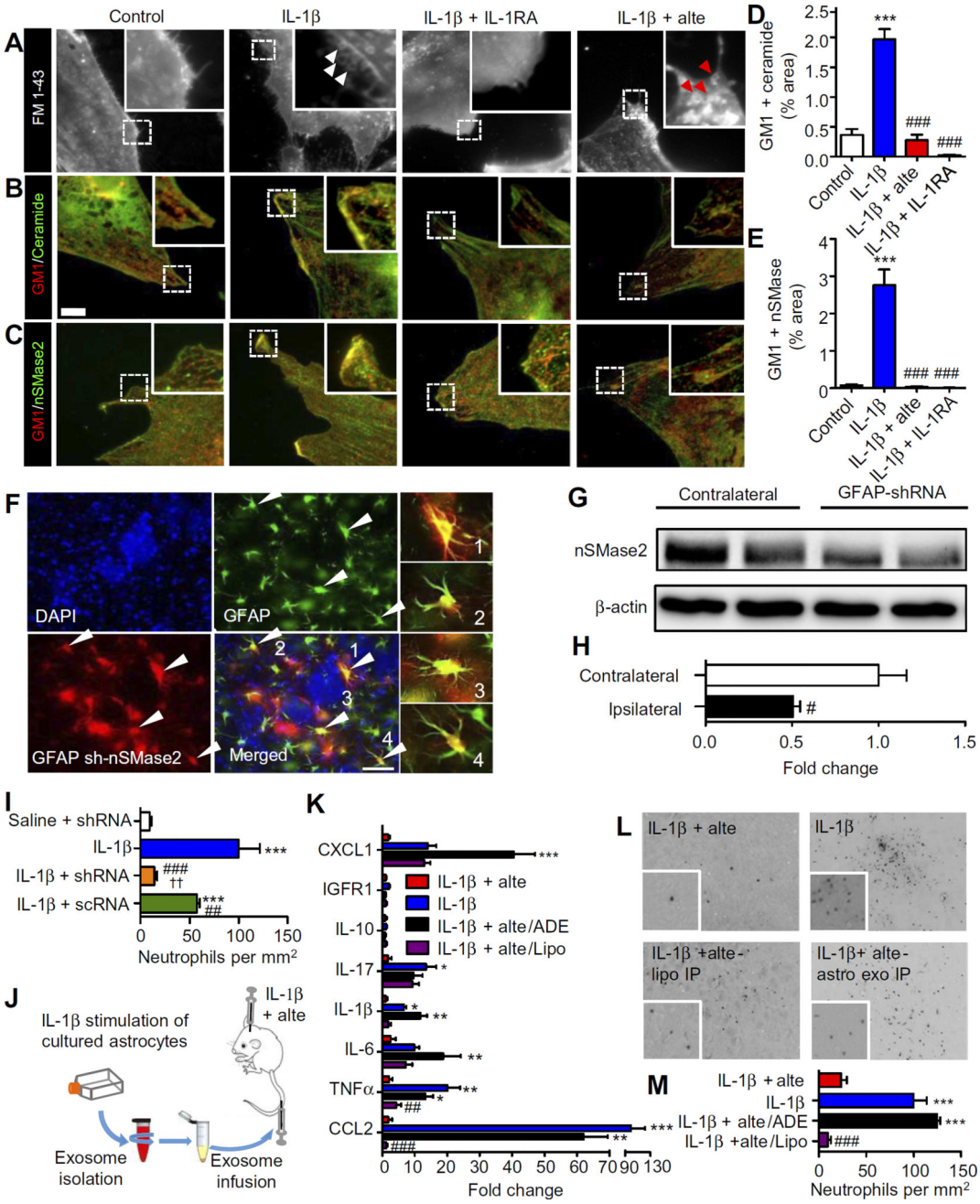

Fig. 3. IL-1β stimulation of astrocytes results in the formation of membrane microdomains that are EV release sites

(**A**) Representative fluorescence images from FM1-43–labeled astrocytes. White arrows represent the release of EVs into the medium; red arrows represent EVs trapped in the cell or not yet released. (**B** and **C**) Representative immunofluorescent overlays of CTx-555 (labels GM1; red) and ceramide (green) dual immunopositive plasma membrane microdomains. Insets: Magnification of the indicated region. Scale bar, 50 μm. (**D** and **E**) Quantitative data of the percentage of plasma membrane dual positive for (D) ceramide and GM1 or (E) nSMase2 and GM1 for the indicated treatment conditions. (**F**) Immunofluorescence images

from mouse striatum 72 hours after injection of an adenoviral vector expressing a GFAP-driven shRNA directed against nSMase2 (GFAP sh-nSMase2; 5×10^9 particles in 0.5 μl). Images of 4′,6-diamidino-2-phenylindole (DAPI), GFAP, the mCherry-expressing vector, and merged image obtained from mouse striatum. Insets: Magnification of the indicated astrocytes. (**G** and **H**) Representative Western blot (G) and quantitation (H) of nSMase2 abundance in the striatum-expressing GFAP sh-nSMase2 and the contralateral striatum. (**I**) Stereological quantitation of $Ly6b^+$ leukocytes in the striatum 24 hours after the injection of saline or IL-1β as indicated. (**J**) Pictorial representation of experimental design for infusions of astrocyte-shed EVs. Astrocytes in fresh plasma-free medium were stimulated with IL-1β for 2 hours. EVs were isolated from the medium, and 2.78×10^9 EVs were infused into the tail vein of mice that were administered IL-1β (0.1 ng in 3 μl) + altenusin (50 μM). (**K**) qRT-PCR data of liver cytokine expression 4 hours after infusions of EVs or control liposomes depleted of protein and RNA for the indicated treatment conditions. (**L** and **M**) Representative photomicrographs (L) and stereological quantifications (M) of $Ly6b^+$ leukocytes in the striatum 24 hours after infusion of astrocyte-shed EVs or liposomes. Data are means ± SEM of 35 to 60 cells from three to four independent experiments per condition for immunofluorescence, $n = 3$ to 5 mice per condition for GFAP sh-nSMase2 expression, PCR, and quantitation of leukocyte influx. $^*P < 0.01$, $^{**}P < 0.05$, $^{***}P < 0.001$ compared to control; $^{\#}P < 0.05$, $^{\#\#}P < 0.01$, $^{\#\#\#}P < 0.001$ compared to IL-1β or contralateral; $^{\dagger\dagger}P < 0.05$ compared to IL-1β + scRNA. ANOVA with Tukey post hoc comparisons.

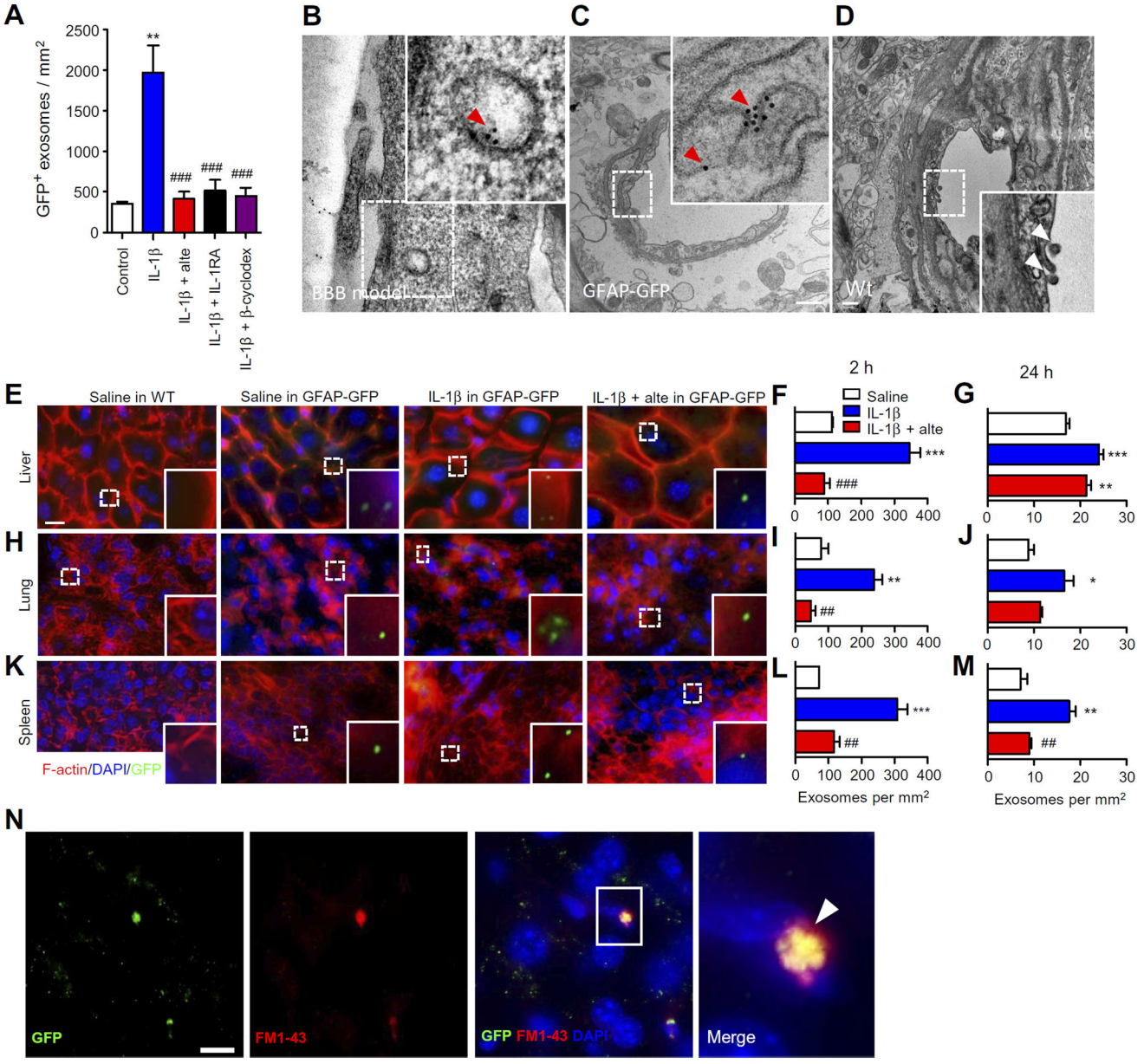

Fig. 4. EVs released from IL-1β–stimulated astrocytes rapidly cross the BBB and localize to peripheral organs

(**A**) Quantification of number of GFP$^+$ particles that were transported through an in vitro model of the BBB under the described conditions. (**B** to **D**) Representative electron micrographs of immunogold-labeled GFP$^+$ EVs located in the cytoplasm of an endothelial cell from the BBB model (B) and in the cytoplasm of vascular endothelial cells of a GFP-GFAP transgenic mouse (C) or a WT mouse (D) after striatal injection of IL-1β. Red arrows indicate immunogold-labeled GFP. Immunogold GFP labeling was not observed in endothelial cells from WT mice, but luminal release of EVs was observed (white arrows). (**E** to **M**) Representative immunofluorescence images (at 2 hours) and stereological quantitation (at 2 or 24 hours) of GFP$^+$ EVs from the liver (E) to (G), lung (H) to (J), and spleen (K) to (M) in the indicated mouse strain after striatal injections of saline, IL-1β, or IL-1β +

altenusin (alte) in the indicated strain. Overlay images show F-actin–labeled cells (red), DAPI-labeled nuclei (blue), and GFP^+ EVs (green). h, hours. (**N**) Immunofluorescence images from the liver of a GFAP-GFP mouse injected in striatum with the membrane probe FM1-43 followed by IL-1β. Images show GFAP, FM1-43, and the merged image with DAPI. Inset: Magnification of the indicated region. Scale bar, 1 μm. Data are means ± SEM of n = 5 culture for BBB and n = 5 mice per condition. $^*P < 0.05$, $^{**}P < 0.01$, $^{***}P < 0.001$ compared to saline; $^{\#\#}P < 0.01$, $^{\#\#\#}P < 0.001$ compared to IL-1β. ANOVA with Tukey post hoc comparisons.

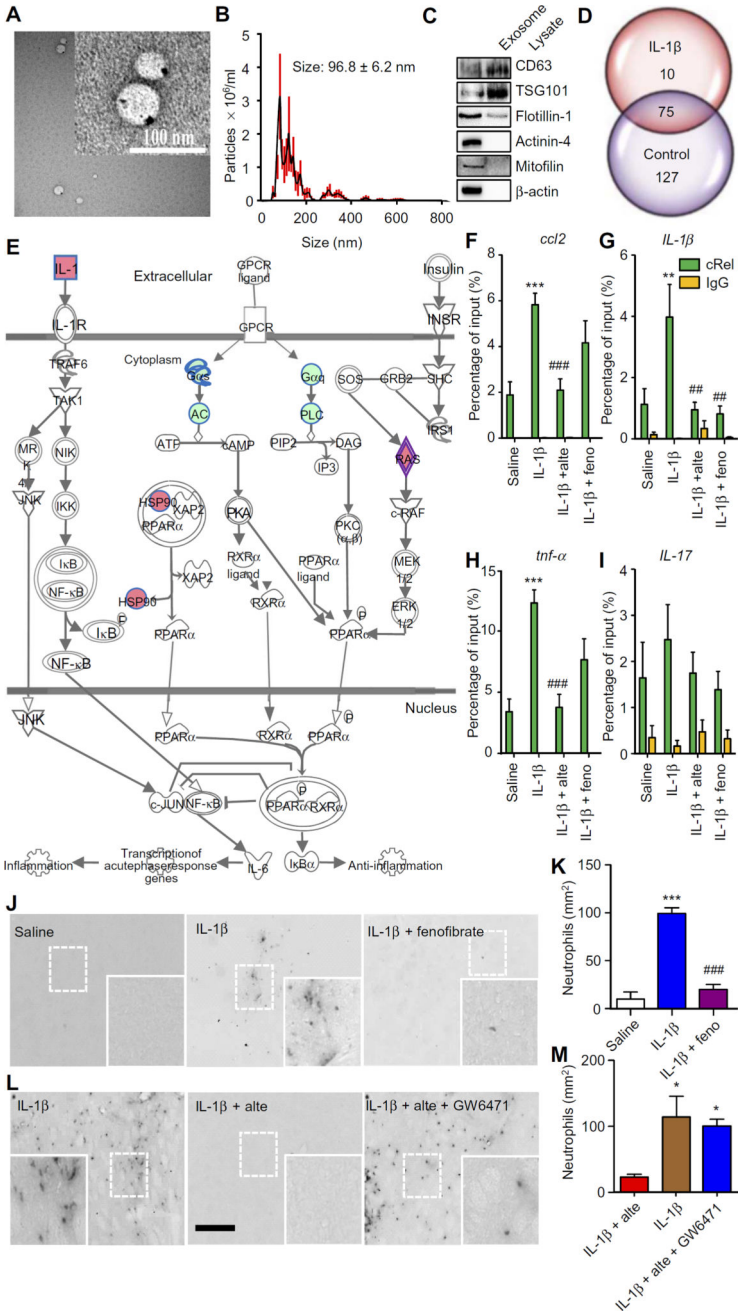

Fig. 5. The cargo of EVs shed from astrocytes in response to IL-1β regulates the liver cytokine response through modulation of PPARα

(**A**) Representative electron micrograph of EVs isolated from astrocytes 2 hours after stimulation with IL-1β (100 ng/ml). (**B**) Quantitation of astrocyte-shed EV size and quantity. (**C**) Representative Western blots from astrocyte-shed EVs stained for the tetraspan protein CD63 and the lipid raft marker flotillin. (**D**) Venn diagram comparing protein content of EVs constitutively released from astrocytes (control) with EVs released 2 hours after stimulation with IL-1β (100 ng/ml). (**E**) IPA was conducted using the protein and miRNA content of astrocyte EVs shed in response to IL-1β. Red fill indicates negative

regulation; green fill indicates positive regulation; blue outline shows components identified by the protein content of EVs; and a double purple outline shows components targeted by multiple miRNAs. (**F** to **I**) ChIP assays results of NF-κB binding to (F) *Ccl2*, (G) *IL-1*β, (H) *TNF*α, and (I) *IL-17* promoter regions in the liver 2 hours after striatal injections of saline or IL-1β (0.1 ng in 3 μl). (**J** and **K**) Representative photomicrographs (J) and stereological quantitation (K) of $Ly6b^+$ leukocytes in the striatum 24 hours after striatal injection of saline, IL-1β, or IL-1β + fenofibrate (PPARα agonist; 10 mg/kg by tail vein infusion). (**L** and **M**) Representative photomicrographs (L) and stereological quantitation (M) of $Ly6b^+$ leukocytes 24 hours after striatal injection of IL-1β, IL-1β + altenusin (50 μM), or IL-1β + altenusin + GW6471 (PPARα antagonist; 20 mg/kg by tail vein infusion). Data are means ± SEM, $n = 3$ to 6 mice per condition. $^{**}P < 0.01$, $^{***}P < 0.001$ compared to saline; $^{*}P < 0.05$ compared to IL-1β + altenusin; $^{\#\#}P < 0.01$, $^{\#\#\#}P < 0.001$ compared to IL-1β. ANOVA with Tukey post hoc comparisons.